New KNbTeO6 transparent tellurate ceramics

Morgane Dolhen, Julie Carreaud, Gaëlle Delaizir, Jean-René Duclère, Marion Vandenhende, Nicolas Tessier-Doyen, Olivier Tantot, Damien Passerieux, Pierre-Eugène Coulon, Philippe Thomas, et al.

New $KNbTeO_6$ transparent tellurate ceramics

Morgane Dolhen[a], Julie Carreaud[a], Gaëlle Delaizir[a], Jean-René Duclère[a], Marion Vandenhende[a], Nicolas Tessier-Doyen[a], Olivier Tantot[b], Damien Passerieux[b], Pierre-Eugène Coulon[c], Philippe Thomas[a], Mathieu Allix[d], Sébastien Chenu[a,*]

[a] Institut de Recherche sur les Céramiques (IRCER), UMR 7315 CNRS, Université de Limoges, Centre Européen de la Céramique, Limoges, France
[b] Xlim, UMR 7252 CNRS, Université de Limoges, France
[c] LSI, CEA/DRF/IRAMIS, École Polytechnique, CNRS, Institut Polytechnique de Paris, F-91128 Palaiseau, France
[d] Conditions Extrêmes et Matériaux : Haute Température et Irradiation (CEMHTI), UPR3079 CNRS, Orléans, France

ARTICLE INFO

Keywords:
Transparent ceramic
Pyrochlore
Spark plasma sintering
Microstructure

ABSTRACT

New transparent defect pyrochlore $KNbTeO_6$ ceramics were successfully prepared by Spark Plasma Sintering (SPS) of same composition polycrystalline powders elaborated by classic solid-state reaction from oxide precursors (K_2CO_3, Nb_2O_5, TeO_2) and followed by high energy milling powders. As such precursors are not available as commercial nanopowders, a suitable process has been developed by combining solid-state reactions and high energy milling. The determination of appropriate consolidation conditions and sintering parameters of the green body such prepared, are described in this paper. The resulting ceramic is transparent in both the visible and near infrared range (up to 5.5 μm). The maximum of transmittance is reached in the near infrared region around 2500 nm with a value of 78 % (1 mm thick sample), close to the maximum theoretical value of transmittance. This transparent $KNbTeO_6$ ceramic demonstrates a homogeneous and dense microstructure with an average grain size less than 500 nm. A small content of secondary phase has been detected by nanoscale observations without drastic effects on transparency. This ceramic exhibits very good mechanical properties similar to the Y_2O_3 transparent ceramic, as well as interesting dielectric properties in the microwave range. This innovative method should drive the development of new transparent materials with technologically relevant applications.

1. Introduction

TeO_2 based-materials present numerous advantages over silicates, especially regarding enlargement of transparency in the infrared region up to 6 μm, lower melting point, higher linear refractive index, better solubility of rare-earth ions for optical emission properties, and excellent nonlinear optical properties [1,2]. Tellurite glasses have been reported to develop optical devices such as white LEDs [3], or with specific emission around 2.7 μm [4], or lasing properties [5,6] and glass fibers for supercontinuum generation [7,8].

Regarding photonic applications, a high crystalline fraction is generally required to ensure a strong crystal field around luminescent ions. Therefore transparent ceramics are interesting and competitive candidates in regards to glasses [9,10]. Compared to single crystals, transparent ceramics are characterized by their relatively shaping easiness, low cost elaboration, wide range of chemical compositions and the possibility to be heavily and homogenously doped [11]. These materials have found commercial applications mainly as gain media for solid-state laser amplifiers [10], scintillators [12], optical lenses [13], medical imaging applications, luminescent laser diodes and transparent armour [14].

Over the last decade, an innovative route has been developed to obtain new transparent ceramics. It consists in full and congruent crystallization from a bulk glass precursor [15–17]. Tellurite transparent ceramic with $Bi_{0.8}Nb_{0.8}Te_{2.4}O_8$ composition has been elaborated by this method [18] and laser emission has been demonstrated with Nd^{3+} in this transparent ceramic [19]. Core-clad crystalline fibers with a similar composition have been finally even more recently elaborated by Wen et al. [20].

Besides tellurites, tellurates also constitute another family of materials which appears to be interesting for their low dielectric losses in the microwave range and for their potential applications in the field of low temperature co-fired ceramic (LTTC) technology. Some examples can be found for instance in the following review dealing with LTCC materials [21].

Nevertheless, specific oxidation states such as Te^{6+} remain

* Corresponding author.
E-mail address: sebastien.chenu@unilim.fr (S. Chenu).

https://doi.org/10.1016/j.jeurceramsoc.2020.04.005
Received 19 February 2020; Received in revised form 1 April 2020; Accepted 2 April 2020

inaccessible in glass [1] and/or limited candidates are available for a full glass crystallization process due the restricted glass forming ability of some compositions. Transparent oxide ceramics are generally prepared by pressure-assisted sintering techniques, such as hot-pressing (HP), hot-isostatic pressing (HIP), or Spark Plasma Sintering (SPS) [22]. SPS is characterized by a super-fast sintering process to consolidate ceramic powders which can become fully dense within several minutes without significant grain growth. These powder sintering procedures have been developed to avoid light-scattering sources in the resulting material. Indeed, a limited residual porosity, as well as secondary phases, leads to a local variation of the refractive index which induces decrease of the material transparency [23]. In order to avoid birefringence problems, transparency in polycrystalline ceramics is generally ensured by optical isotropy (i.e. cubic symmetry). For example, different classes of cubic transparent oxide ceramics have been reported: garnets [10] ($Y_3Al_5O_{12}$, $Lu_3Al_5O_{12}$), sesquioxides [24,25] (Y_2O_3, Lu_2O_3), spinels [26] ($MgAl_2O_4$, $ZnAl_2O_4$), defect-fluorites [27,28] (Lu_3NbO_7, Gd_3TaO_7) and ZrO_2 [13].

In the case of anisotropic materials, the transparency is limited by the intrinsic birefringence of the material which gives rise to light scattering effects at grain boundaries. This light scattering effect is amplified with the increase of crystallite size. To prevent this effect to decrease the transparency in ceramics, Sato et al., have reported the possibility to orientate the crystallites by applying a strong magnetic field during the sintering process [29]. However, this innovative approach is quite difficult to use and the crystallites needs to be sensitive to magnetic fields which limits the development of this technique. In some cases, sintering additives, such as SiO_2 and LiF, are added to ceramic powders before the sintering step. Indeed, the presence of a viscous phase enhances densification by particle rearrangement during the sintering and the transparency of the final ceramic could be improved [30].

To overcome the drawbacks of light scattering in ceramic materials, specific nanometer-scale raw materials are generally employed and several authors also use commercial nano-powders of the final composition. No such commercial powders are available for TeO_2 based materials, so raw materials must be designed to improve their sintering process.

In this work, we report the elaboration of a new tellurate transparent ceramic, $KNbTeO_6$, by spark plasma sintering of powders with same composition elaborated by solid-state reaction and further high-energy milling. $KNbTeO_6$ is a cubic phase with defect pyrochlore structure [31] and to the best of our knowledge, this compound has never been elaborated as a transparent ceramic but only as ceramic powders. The synthesis method is described, the development of a suitable powder and the determination of appropriate conditions for powder consolidation and sintering with limited carbon contamination are the main technological challenges. The transmittance in both the visible and IR ranges is measured and discussed in light of the microstructure (crystals size, porosity, and grain boundaries thickness) determined by SEM and TEM. Mechanical and microwave dielectric properties have been also evaluated.

2. Experimental

2.1. Materials synthesis

The $KNbTeO_6$ composition was synthesized in an alumina crucible from high purity precursors (TeO_2 Alfa Aesar 99.99 %, Nb_2O_5 Sigma Aldrich 99.9985 %, K_2CO_3, $1.5H_2O$ Fluka Analytical 99.995 %) using solid-state reaction under air. A ~ 30 g mixture was prepared by finely mixing raw powders in an agate mortar with ethanol to ensure homogeneous repartition. The powder was then fired in air at 600 °C for 2 h. The obtained sample was then finely ground, homogenized, and finally sintered in air at 750 °C for 2 h.

The milling procedure was then carried out in an attrition mill system with vertical configuration. One of the characteristics of attrition mills is that the Teflon milling chambers are not rotated during the milling [22]. The powders were stirred vigorously by a Teflon stirrer with zirconia balls of 3 mm of diameter for 2 h dispersed in 200 mL of ethanol. The milling speed was set at 1000 rpm. Then, different sizes of ZrO_2 ball milling were used: 1 mm for 2 h and finally 0.5 mm for 4 h. The suspension was filtered with a 100 μm sieve to remove zirconia balls and dried at 100 °C to remove ethanol. The resulting powder was finally calcined at 400 °C in air for 6 h and was then ready for spark plasma sintering.

3. SPS sintering

Spark plasma sintering equipment (Dr. Sinter 825 Syntex machine (Fuji FDC, Japan)) was used to sinter and densify the ceramic powders previously obtained. Different protocols were tested to optimize the sintering. The $KNbTeO_6$ attrited powder was introduced in an 8-mm-diameter graphite die. For all the SPS attempts, the temperature was measured with a thermocouple positioned at the close vicinity of the sample, through the die. No sintering aids or additives were used. The temperature was increased to 550 °C within 7 min under argon atmosphere. The dwell time for all experiments was 20 min. A uniaxial pressure of 100 MPa was progressively loaded in 1 min at the beginning of the heat treatment and kept constant until a temperature of 550 °C during 20 min. The cooling of sample took 3 min down to room temperature.

4. Characterization methods

XRPD data were recorded on a Bragg Brentano D8 Advance Bruker diffractometer (CuKα radiation) equipped with a LynxEye XE detector over an angular range of $10^\circ < 2\theta < 70^\circ$ for phase identification and of $5^\circ < 2\theta < 130^\circ$ using a 0.012 step size for structural refinements. These latter were performed using the Rietveld [32] method implemented in the JANA2006 [33] software.

Thermogravimetric analyses were performed on a Setaram LabSys Evo apparatus on ceramic powder recovered after attrition procedure using a heating rate of 10 °C/min. up to 500 °C in air.

Particle size analysis was performed by laser diffraction granulometry (Horiba Partica La-950). The powder was dispersed in deionized water by sonication for 15 min.

The microstructure of ceramic powders and a polished sintered ceramic was observed using a Quanta 450 FEG scanning electron microscope. The density of the samples was measured at room temperature using Archimedes method with absolute alcohol as immersion fluid. The error in the determination of the density is ± 0.02 g cm^{-3}.

High-resolution transmission electron microscopy (HR-TEM), selected-area electron diffraction (SAED), and scanning transmission electron microscopy (STEM) were performed on a JEOL 2010F operating at 200 kV and a Titan Themis (200 kV, probe-corrected, probe size 0.1 nm). STEM-High-Angle Annular Dark Field (STEM-HAADF) imaging, energy-dispersive X-ray spectroscopy (EDX) analysis were carried. The ceramics were prepared prior to (S)TEM observations by focused ion beam (FIB, FEI Scios).

Optical transmission measurements were carried out within the 300–3300 nm range, with the sample placed at normal incidence, using a Varian Cary 5000 spectrophotometer operated in a dual beam configuration and in the infrared range using a Thermo Scientific Nicolet 6700 FTIR spectrophotometer.

The diffuse reflectance data were acquired for $KNbTeO_6$ powders using an integration sphere. Such data were then treated using the Kubelka–Munk formula in order to extract the optical band gap. It is noteworthy that the condition for the application of such formula requires controlling that the population of selected grains remains with sizes larger than 5 μm (condition strictly satisfied for the starting raw $KNbTeO_6$ powder, but not for the attrited powder (see further)).

The linear refractive index n of the samples was extracted from ellipsometry measurements, performed using a Horiba Jobin-Yvon UVISEL Extended Range spectroscopic ellipsometer operated in the 225 − 850 nm range. The angle of incidence was fixed at 65° (close to the Brewster angle) and the light spot size was 1 mm in diameter.

Concerning mechanical properties, the hardness (H) was determined on mirror polished surfaces using a diamond Vickers indenter (Buelher MicroMet 6040) for a load of 50 g during 15 s. The elastic properties (Young's modulus E, shear modulus G, and Poisson's ratio ν) were determined by pulse echography technique operating in infinite medium mode at 10 MHz on a 8 mm diameter disc-shaped specimen exhibiting a thickness of 1.2 mm

Microwave dielectric properties (permittivity and losses) were extracted via a resonant method described in details in Ref. [34], where the dielectric resonator is placed inside a cylindrical cavity in copper. For such measurements, series of dense $KNbTeO_6$ ceramic pellets were specifically prepared. Finally, the resonance frequency was found close to 5 GHz, after taking into account all the following parameters (i.e. the contributions of the copper cavity plus that of the sample support made of Teflon, and of course the $KNbTeO_6$ dielectric resonator (here, the accurate dimensions of the $KNbTeO_6$ pellet are: Diameter = 8 mm and Thickness = 4 mm)).

5. Results and discussions

As shown in Fig. 1, the X-ray powder diffraction patterns of $KNbTeO_6$ ceramic powders obtained after the two steps solid-state reaction process present a perfect match with the cubic defect pyrochlore $KNbTeO_6$ structure (PDF 04-005-6055). The position of the peaks corresponds to the theoretical $KNbTeO_6$ diffractogram with a Fd-3 m cubic defect pyrochlore structure (a = 10.25 Å). No secondary crystalline phase was detected. The solid-state reaction was realized under air to ensure the complete oxidation of Te^{4+} into Te^{6+} [31,35]. Indeed, TeO_2 (i.e. Te^{4+}) is used as tellurium precursor and its valence is increased during this solid-state reaction thanks to the presence of oxygen which induces the formation of this tellurate (Te^{6+}) phase. The obtained $KNbTeO_6$ powder has a slight beige colour, as reported by [36].

The particle size has been estimated by laser granulometry, as illustrated in Fig. 2. After solid-state reactions, the tellurate powder exhibits a bimodal size distribution with two peaks centered at 15 and 300 µm. Agglomerated powder is detrimental for the sintering process since it can contribute to later formation of pores, and a powder with reduced

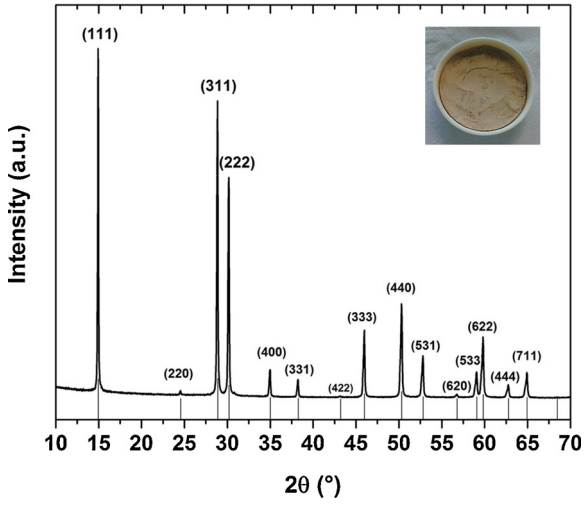

Fig. 1. XRD patterns of the defect pyrochlore $KNbTeO_6$ ceramic powder prepared at 750 °C under air during 2 h. The indexation corresponds to the $KNbTeO_6$ reported structure (PDF 04-005-6055). A photograph of the ceramic powder in an alumina crucible is also shown in insert.

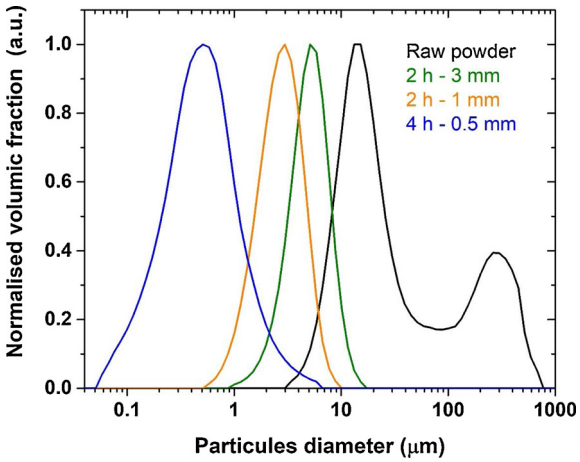

Fig. 2. Particle size distribution of $KNbTeO_6$ powder before (black curve) and after attrition process with zirconia balls with diameter of 3 mm (green), 1 mm (orange) and 0.5 mm (blue). (For interpretation of the references to colour in this figure legend, the reader is referred to the web version of this article.)

particle size is usually beneficial for densification [22]. Therefore, attrition has been performed to reduce aggregates size. After 2 h of attrition with 3 mm ZrO_2 balls, the size distribution (grains in suspension) shows a single mode centered at 5 µm. By reducing the zirconia ball size down to 0.5 mm diameter, a strong shift towards smaller particle size is observed. The resulting powder exhibits a monomodal particle size distribution centered at 500 nm. The particle size distribution in number (Fig. 4-b)) is centered on 70 nm.

To go further in the powder characterizations, the morphology of the $KNbTeO_6$ powders has been studied by SEM (Fig. 3). The powder obtained directly by solid-state reaction presents a submicronic particle size around 1 or 2 µm, strongly aggregated. The crystallites exhibit angular shapes, in agreement with the cubic structure of this $KNbTeO_6$ compound. After attrition, the morphology of the final powder is totally modified with finer particles.

Thermogravimetric analysis has been performed on dried $KNbTeO_6$ powder after attrition process (Fig. 4-a). One can note a slight decrease of weight loss during the heat treatment up to 400 °C. This phenomenon could be attributed to a Teflon residue deriving from the milling procedure realized in Teflon media or impurities from ethanol. Above 400 °C, there is no more weight loss. From these observations, the attrited powder was calcined for 6 h at 400 °C in a muffle furnace to remove these impurities. No changes have been detected by XRD measurements after this post-treatment of the powder (data not shown here). Only the cubic $KNbTeO_6$ phase was observed. Particle size distribution is increased during this heat treatment with a monomodal particle size distribution of the agglomerates centered on 6 µm. It can be observed that the particle size distribution in number (Fig. 4-b) is centered on 1 µm which is confirmed with SEM observations.

Fig. 5 shows the visual aspect of the $KNbTeO_6$ sample sintered by SPS during 20 min at 550 °C (1 mm thickness) and optically polished. The ceramic appears transparent in the visible range, with a red coloration. No carbon contamination has been observed contrary to the case of sintered tellurite glasses by SPS [37]. The transparency range of this tellurate ceramic extends from 0.7 up to 5.5 µm. The maximum of transmission is reached in the near infrared region, around 2500 nm, with a value of 78 %.

In addition, the chromatic dependence of the refractive index was measured on the same sample by spectroscopic ellipsometry. Using the well-known Sellmeier dispersion expression, it was also possible to correctly fit the refractive index values in the 290 − 850 nm wavelength range. This allowed us extracting the refractive index at infinite wavelength (where there is no more chromatic dispersion), which was found close to 1.96.

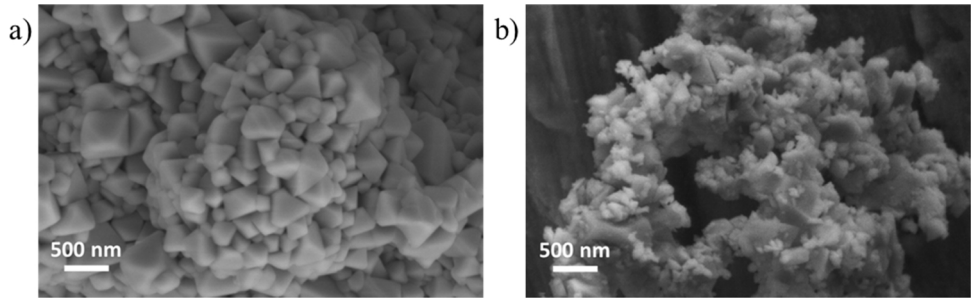

Fig. 3. SEM observations of $KNbTeO_6$ powder before (a) and after (b) complete attrition process.

Approximating that most of light reflection occurs at the two air/ceramic interfaces (i.e. neglecting the contribution of multiple reflections), the following relationship can be expressed between n and T (the transmission coefficient) in the transparent region: $T = (2n)/(n^2+1)$.

Injecting finally the above refractive index value of 1.96 into the previous equation leads to derive a maximum theoritical value for the transmission, which is estimated to be 81 %.Thus, the maximum of 78 % reached experimentally is so far pretty good, but there is still some room for improvement.

Besides this slight difference of transmission, the shape of the transmission curve also reflects a limited presence of light scattering sources such as porosity or secondary phases. To gain more information regarding this subject, the structure and the microstructure of the SPS densified ceramic have been studied.

First, X-ray powder diffraction data were acquired from a crushed $KNbTeO_6$ transparent ceramic. The XRD pattern looks completely similar to the one collected on starting powders (either raw or attrited), therefore testifying that the SPS process does not affect the crystal structure. Then, a Rietveld refinement was performed using the Fd-3 m cubic defect pyrochlore structural model previously reported [38] as a starting point (1 K crystallographic site on 32e position (x,x,x), 1 mixed Nb/Te site on a 16d position (1/2,1/2,1/2) and 1 O site on a 48f position (x,1/8,1/8)). The refinement converged easily with cell parameter a = 10.2519(1) Å. The refined XRPD data (agreement factors WRp = 8.16 % and GOF = 5.48) are presented in Fig. 6 and the resulting parameters (x = 0.1049(7) for the K position and x = 0.4302(2) for the O position, leading to Nb/Te-O bond lengths of 1.948(1)) are very close to the literature. A view of the structure, showing $(Nb/Te)O_6$ octahedra sharing corners to form a three dimensional framework possessing tunnels running down the axes in which the K cations are located, is embedded (Fig. 6). A very minor secondary phase could be detected (see black stars) but could not be identified.

One can note that SEM observations (Fig. 7-a) reveal a typical nanostructure of ceramic obtained by powder densification. The average grain size is around 500 nm and no porosity was detected during these observations. Using Archimedes method, the density of the $KNbTeO_6$ ceramic was estimated to 4.38 g cm^{-3}. Compared to the density mentionned in Ref. [39] and the experimental value determined by Rietveld affinement (i.e. 4.385 g cm^{-3}), we could conclude that the sintered $KNbTeO_6$ ceramic is fully dense. SEM-EDX analysis has been performed to detect the presence of impurities due to the attrition process but there was no evidence of the presence of zirconia. Morever, one can read the text through the sample which attests very limited light scaterring in this ceramic. In the same way, the band gap of the ceramic appears abrupt, confirming this phenomena. The sample was then polished and prepared by FIB-SEM prior to TEM observations in order to get volume information.

STEM-HAADF observations show the quasi absence of nanometer scale pores (annoted by black arrow on Fig. 7-b and -c) which is in agreement with density measurement. Moreover, the grain size, inferior to 0.5 µm, is in agreement with SEM characterizations. STEM-HAADF

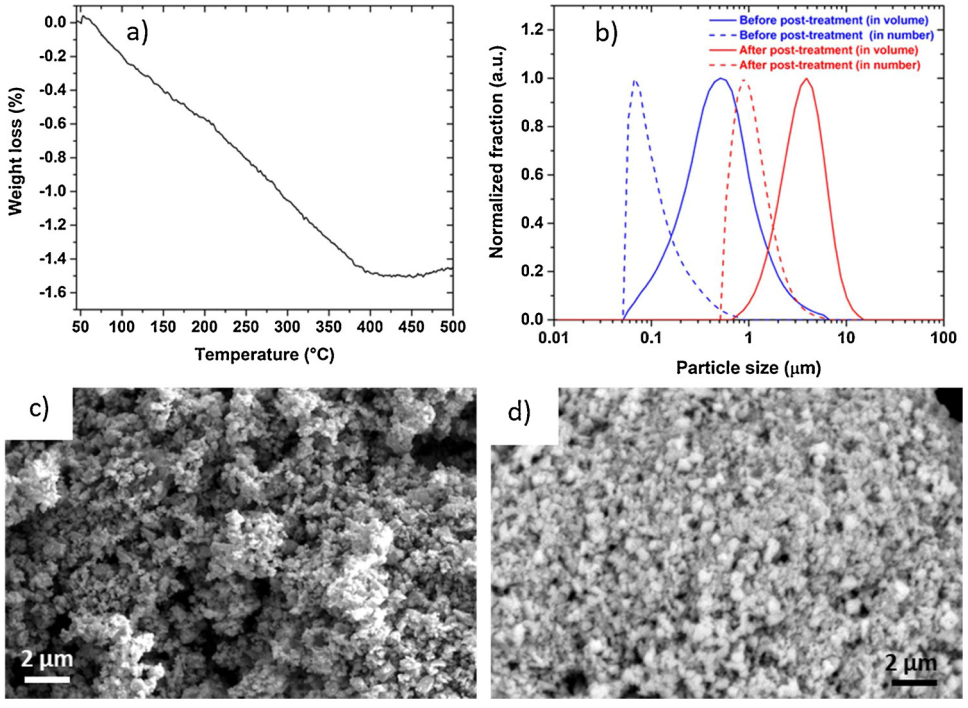

Fig. 4. a) TGA performed on $KNbTeO_6$ powder after complete attrition. b) Particle size distribution of $KNbTeO_6$ attrited powder before (blue) and after (red) pre-treatment at 400 °C during 6 h. The respective SEM observations are presented in c) and d). (For interpretation of the references to colour in this figure legend, the reader is referred to the web version of this article.)

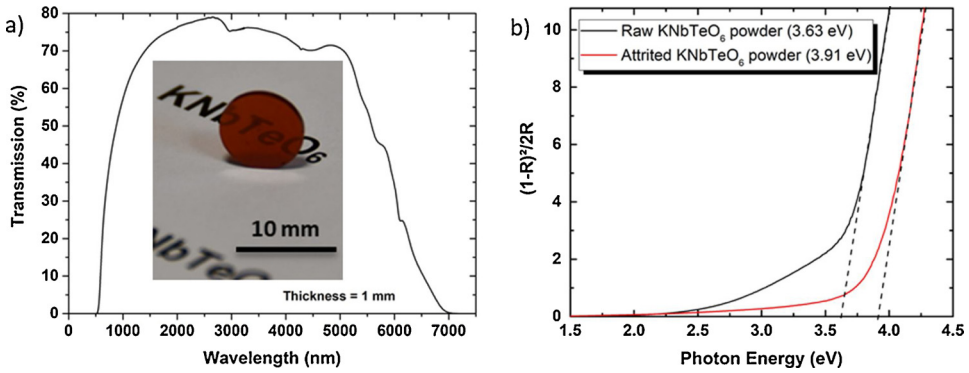

Fig. 5. a) Optical transmission spectra of the $KNbTeO_6$ ceramic densified by SPS and a photograph of the material is also shown. (Thickness = 1 mm). b) Kubelka-Munk plot of $KNbTeO_6$ raw powder (black curve) and attrited powder (black curve).

images show a nanostructure consisting of grains of two distinct types: areas with dark contrast were assigned to $KNbTeO_6$ whereas areas with bright contrast must be related to a different phase with higher Z values (one should note that, contrary to the TEM images, the contrast of STEM-HAADF images is directly linked to the atomic number Z). Consequently, the bright areas, which are present in very limited quantities and in areas smaller than 100 nm, must be enriched in Te and/or Nb. The heavy secondary phase appears to be present in the sintered ceramic but its proportion is very low in agreement either with the presence of two minor extra reflections (annoted by black stars in Fig. 6) on XRD measurements or with the shape of the transmission curve, attesting the limited presence of light scattering sources.

In order to characterise and to understand the coloration of the sintered ceramic, the value of the band gap (Eg) was estimated according to UV absorption edge. The value of Eg is about 2.4 eV, which falls in agreement with the red color of the ceramic (cf. Fig. 5-a). However, raw and attrited powders show respectively some beige (cf. Fig. 1) and light beige colours (not shown here). As testified by Fig. 5-b, from the diffuse reflectance measurements, it was possible to derive the value for the optical band gap, by applying the Kubelka–Munk formula: $F(R) = (1\text{-}R)^2/2R$, with R being the reflection coefficient. Respective values of 3.63 and 3.91 eV were extracted for the raw and attrited powders. Such values (especially the one for the raw powder) are in rather good agreement with was recently published in [36]. Thus, the 2.4 eV value measured for the final sintered ceramic appears surprising and in contradiction with the data collected for powders (as the crystal structure remains unchanged by the SPS process). Indeed, based on the aforementioned Eg values of $KNbTeO_6$ powders, one would expect the final ceramic to be transparent in the complete visible range, and as a consequence to be colourless. Therefore, our current assumption is that the red colour might be connected to this unidentified secondary phase, even though the latter is present in very limited proportions.

As well, another explanation for the coloration of this ceramic could be the existence of a mixed valence of Te. Indeed, as reported for cesium tellurium oxide ($CsTe_2O_{6\text{-}x}$ phases) [40], the presence of both Te^{4+} and Te^{6+} in the same compound can induce red coloration. As the sintering process is performed in graphite environment, occurrence of partial reduction of tellurium can be assumed. However, X-ray photoelectron spectrometry (XPS) performed on the sintered $KNbTeO_6$ transparent ceramic only showed the presence of Te^{6+}, as also reported recently [36]. Therefore, the red colour is probably not explained by different oxydation states for Te, even though the presence of a very limited amount of Te^{4+} (below the detection limit of the XPS set-up) cannot be completely excluded and modified the coloration of ceramic.

The mechanical and dielectric properties of the new $KNbTeO_6$ transparent ceramic have been studied and summarized in Table 1. The Young's modulus value (193 GPa) is quite high compared to the other transparent polycristalline $Bi_{0.8}Nb_{0.8}Te_{2.4}O_8$ ceramic obtained by full cristallization of glass [18], and similar to the transparent Y_2O_3 refractory ceramic [41]. Vickers hardness of the ceramic exhibits a value as high as 5.5 GPa, which is more than a quarter of the hardness value of the polycrystalline $Bi_{0.8}Nb_{0.8}Te_{2.4}O_8$ ceramic. These observations are directly linked to the microstructure of this ceramic, which presents an average grain size around 500 nm.

Dielectric properties were also measured in the microwave range (at 5 GHz). The relative dielectric permittivity ($\varepsilon_r = 56$) measured for the $KNbTeO_6$ ceramic appears among the high values reported for materials potentially devoted to the LTCC technology [21], and is therefore

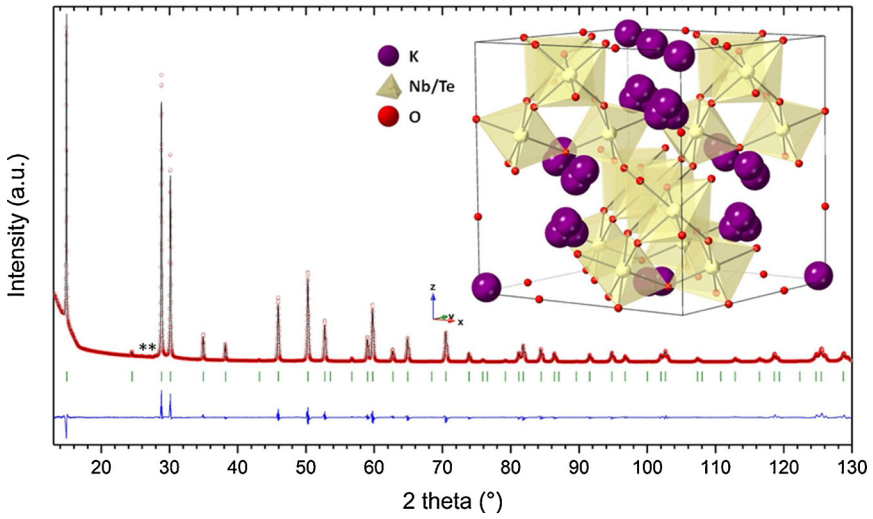

Fig. 6. Rietveld plot from X-ray powder diffraction data recorded from a grounded transparent $KNbTeO_6$ ceramic at room temperature (experimental data, simulated diagram and difference curve correspond to red circles, black solid line and blue solid line respectively, vertical green ticks correspond to indexations). Reliability factors are WRp = 8.16 % and GOF = 5.48. An unknown minor secondary phase has been detected (black stars). A view of the $KNbTeO_6$ structure is embedded. (For interpretation of the references to colour in this figure legend, the reader is referred to the web version of this article.)

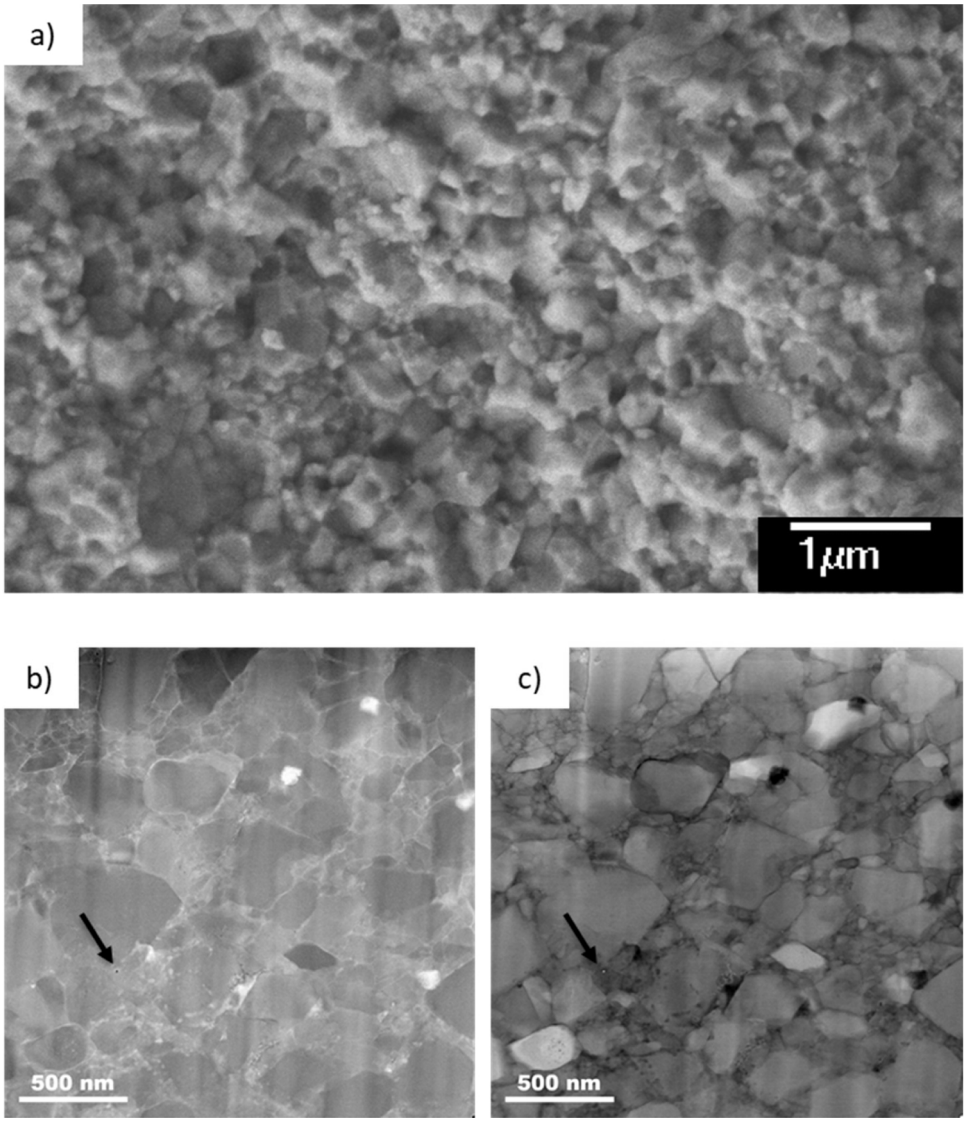

Fig. 7. a) SEM image of a fractured surface of the $KNbTeO_6$ ceramic. b) STEM-HAADF image of the same ceramic and c) same image TEM bright field (BF) mode. A black arrow has been added to point out the presence of a nanometer pore.

Table 1
Mechanical and dielectric properties of the $KNbTeO_6$ ceramic.

Young's modulus, E (GPa)	Poisson's ratio, υ	Hardness (GPa)	Relative dielectric permittivity, ε	Dielectric losses, tanδ
192.8 ± 2.9	0.18 ± 0.01	5.5 GPa	56	2.10^{-3}

interesting in terms of potential applications (especially as filter). For instance, our value is completely similar to that measured by Udovic et al., in the case of the Bi_2TeO_6 phase obtained by solid-state synthesis in the TeO_2-Bi_2O_3 system, under an oxygen atmosphere [42]. However, our dielectric losses (2.10^{-3}) remain so far a bit too high for high performances of resonant microwave component but are still of interest for compact systems such as duplexers, filters and cellular base stations. Future work will attempt to eliminate such secondary phase, as its presence might also affect the dielectric losses.

6. Conclusion

We have demonstrated the possibility to obtain new highly transparent ceramics $KNbTeO_6$ by combining attrition process from $KNbTeO_6$ powders synthesized by classic solid-state reaction and SPS sintering. The resulting ceramics present a dense and homogeneous microstructure with an average grain size of less than 500 nm. This microstructure confers to this material very good mechanical properties similar to transparent Y_2O_3 ceramic but also interesting dielectric properties in the microwave range. This innovative material is transparent in the second atmospheric window (mid wavelength infrared), i.e., the 3 − 5 µm region and may find various applications such as infrared lenses for thermal imaging cameras which is of great importance for night driving assistance, quality control, military or civil applications, and medical imaging applications. This method should drive the development of new transparent materials with technologically relevant applications.

Declaration of interests

The authors declare that they have no known competing financial interests or personal relationships that could have appeared to influence the work reported in this paper.

Acknowledgements

This work benefited from government support managed by the National Research Agency under the Investments for the future program with the reference ANR-10-LABX-0074-01 Sigma-LIM. This work was also supported by the French ANR research program "Investissements d'avenir" (ANR-10-EQPX-50) and benefited of a financial support via the TRAFIC project (ANR-18-CE08-0016-01)

References

[1] R. El-Mallawany, M.D. Abdalla, I.A. Ahmed, New tellurite glass: optical properties, Mater. Chem. Phys. 109 (2–3) (2008) 291–296.
[2] J.E. Stanworth, Tellurite glasses, Nature 169 (4301) (1952) 581–582.
[3] R. El-Mallawany, Tellurite Glass Smart Materials: Applications in Optics and Beyond, (2018).
[4] X. Fan, K. Li, X. Li, P. Kuan, X. Wang, L. Hu, Spectroscopic properties of 2.7Mm emission in Er^{3+} doped telluride glasses and fibers, J. Alloys. Compd. 615 (0) (2014) 475–481.
[5] C. Yao, C. He, Z. Jia, S. Wang, G. Qin, Y. Ohishi, W. Qin, Holmium-doped fluorotellurite microstructured fibers for 2.1μm lasing, Opt. Lett. 40 (20) (2015) 4695–4698.
[6] J. Carreaud, A. Labruyère, H. Dardar, F. Moisy, J.R. Duclère, V. Couderc, A. Bertrand, M. Dutreilh-Colas, G. Delaizir, T. Hayakawa, A. Crunteanu, P. Thomas, Lasing effects in new Nd^{3+}-doped TeO_2–Nb_2O_5–WO_3 bulk glasses, Opt. Mater. 47 (2015) 99–107.
[7] M. Klimczak, D. Michalik, G. Stępniewski, T. Karpate, J. Cimek, X. Forestier, R. kasztelanic, D. Pysz, R. Stępień, R. Buczyński, Coherent supercontinuum generation in tellurite glass regular lattice photonic crystal fibers, J. Opt. Soc. Am. B 36 (2) (2019) A112–A124.
[8] I. Savelii, J.C. Jules, G. Gadret, B. Kibler, J. Fatome, M. El-Amraoui, N. Manikandan, X. Zheng, F. Désévédavy, J.M. Dudley, J. Troles, L. Brilland, G. Renversez, F. Smektala, Suspended core tellurite glass optical fibers for infrared supercontinuum generation, Opt. Mater. 33 (11) (2011) 1661–1666.
[9] R. Won, Ceramic future, Nat. Photonics 2 (4) (2008) 216–217.
[10] A. Ikesue, Y.L. Aung, Ceramic laser materials, Nat. Photonics 2 (12) (2008) 721–727.
[11] A. Goldstein, A. Krell, Transparent ceramics at 50: progress made and further prospects, J. Am. Ceram. Soc. (2016) 1–25.
[12] N.J. Cherepy, J.D. Kuntz, Z.M. Seeley, S.E. Fisher, O.B. Drury, B.W. Sturm, T.A. Hurst, R.D. Sanner, J.J. Roberts, S.A. Payne, Transparent ceramic scintillators for gamma spectroscopy and radiography, Proc. SPIE 7805 (2010), https://doi.org/10.1117/12.862503 78050I-78050I.
[13] U. Peuchert, Y. Okano, Y. Menke, S. Reichel, A. Ikesue, Transparent cubic-ZrO2 ceramics for application as optical lenses, J. Eur. Ceram. Soc. 29 (2) (2009) 283–291.
[14] A. Goldstein, A. Goldenberg, Y. Yeshurun, M. Hefetz, Transparent $MgAl_2O_4$ spinel from a powder prepared by flame spray pyrolysis, J. Am. Ceram. Soc. 91 (12) (2008) 4141–4144.
[15] X. Ma, X. Li, J. Li, C. Genevois, B. Ma, A. Etienne, C. Wan, E. Véron, Z. Peng, M. Allix, Pressureless glass crystallization of transparent yttrium aluminum garnet-based nanoceramics, Nat. Commun. 9 (1) (2018) 1175.
[16] K. Al Saghir, S. Chenu, E. Véron, F. Fayon, M.R. Suchomel, C. Genevois, F. Porcher, G. Matzen, D. Massiot, M. Allix, Transparency through structural disorder: a new concept for innovative transparent ceramics, Chem. Mater. 27 (2) (2015) 508–514.
[17] M. Allix, S. Alahrache, F. Fayon, M. Suchomel, F. Porcher, T. Cardinal, G. Matzen, Highly transparent $BaAl_4O_7$ polycrystalline ceramic obtained by full crystallization from glass, Adv. Mater. 24 (41) (2012) 5570–5575.
[18] A. Bertrand, J. Carreaud, S. Chenu, M. Allix, E. Véron, J.-R. Duclère, Y. Launay, T. Hayakawa, C. Genevois, F. Brisset, F. Célarié, P. Thomas, G. Delaizir, Scalable and formable tellurite-based transparent ceramics for near infrared applications, Adv. Opt. Mater. 4 (10) (2016) 1482–1486.
[19] M. Dolhen, M. Tanaka, V. Couderc, S. Chenu, G. Delaizir, T. Hayakawa, J. Cornette, F. Brisset, M. Colas, P. Thomas, J.-R. Duclère, Nd^{3+}-doped transparent tellurite ceramics bulk lasers, Sci. Rep. 8 (1) (2018) 4640.
[20] S. Wen, Y. Wang, B. Lan, W. Zhang, Z. Shi, S. Lv, Y. Zhao, J. Qiu, S. Zhou, Pressureless crystallization of glass for transparent nanoceramics, Adv. Sci. (2019) 1901096.
[21] M.T. Sebastian, H. Wang, H. Jantunen, Low temperature co-fired ceramics with ultra-low sintering temperature: a review, Curr. Opin. Solid State Mater. Sci. 20 (3) (2016) 151–170.
[22] L.B. Kong, Y.Z. Huang, W.X. Que, T.S. Zhang, S. Li, J. Zhang, Z.L. Dong, D.Y. Tang, Transparent Ceramics, Springer International Publishing, 2015.
[23] R. Apetz, M.P.B. van Bruggen, Transparent alumina: a light-scattering model, J. Am. Ceram. Soc. 86 (3) (2003) 480–486.
[24] Y. Sun, S. Shimai, X. Peng, G. Zhou, H. Kamiya, S. Wang, Fabrication of transparent Y_2O_3 ceramics via aqueous gelcasting, Ceram. Int. 40 (6) (2014) 8841–8845.
[25] D. Zhou, Y. Shi, J. Xie, Y. Ren, P. Yun, Fabrication and luminescent properties of Nd^{3+}-Doped Lu_2O_3 transparent ceramics by pressureless sintering, J. Am. Ceram. Soc. 92 (10) (2009) 2182–2187.
[26] A.V. Belyaev, I.I. Evdokimov, V.V. Drobotenko, A.A. Sorokin, A new approach to producing transparent $ZnAl_2O_4$ ceramics, J. Eur. Ceram. Soc. 37 (7) (2017) 2747–2751.
[27] L. An, A. Ito, T. Goto, Fabrication of transparent Lu_3NbO_7 by spark plasma sintering, Mater. Lett. 65 (19–20) (2011) 3167–3169.
[28] C. Ching-Fong, Ron A. Synowicki, Michael J. Brand, Eric L. Tegtmeier, J.D. Montalvo, Jacob Ivy, Geoff L. Brennecka, Zach Seeley, Nerine J. Cherepy, Steven A. Payne, Processing and characteristics of transparent Gd_3TaO_7 polycrystalline ceramics, J. Am. Ceram. Soc. 101 (5) (2018) 1847–1856.
[29] Y. Sato, J. Akiyama, T. Taira, Orientation control of micro-domains in anisotropic laser ceramics, Opt. Mater. Express 3 (6) (2013) 829–841.
[30] M. Rubat du Merac, H.-J. Kleebe, M.M. Müller, I.E. Reimanis, Fifty years of research and development coming to fruition; unraveling the complex interactions during processing of transparent magnesium aluminate ($MgAl_2O_4$) spinel, J. Am. Ceram. Soc. 96 (11) (2013) 3341–3365.
[31] B. Darriet, M. Rat, J. Galy, P. Hagenmuller, Sur quelques nouveaux pyrochlores des systemes MTO_3-WO_3 et MTO_3 -TeO_3 (m = K, Rb, Cs, Tl; t = Nb, Ta), Mater. Res. Bull. 6 (12) (1971) 1305–1315.
[32] H.M. Rietveld, A profile refinement method for nuclear and magnetic structures, J. Appl. Crystallogr. 2 (2) (1969) 65–71.
[33] V. Petricek, M. Dusek, L. Palatinus, Crystallographic computing system JANA2006: general features, Z. Kristallogr. Cryst. Mater. 229 (5) (2014) 345–352.
[34] D.D. Marco, K. Drissi, N. Delhote, O. Tantot, P.M. Geffroy, S. Verdeyme, T. Chartier, Dielectric properties of pure alumina from 8GHz to 73GHz, J. Eur. Ceram. Soc. 36 (14) (2016) 3355–3361.
[35] T. Komatsu, K. Shioya, Role of Te valence on phases crystallized in K_2O–Nb_2O_5–TeO_2 glasses, J. Non. Solids 209 (3) (1997) 305–308.
[36] A. Waehayee, P. Watthaisong, S. Wannapaiboon, N. Chanlek, H. Nakajima, J. Wittayakun, S. Suthirakun, T. Siritanon, Effects of different exchanging ions on the band structure and photocatalytic activity of defect pyrochlore oxide: a case study on $KNbTeO_6$, Catal. Sci. Technol. (2020).
[37] A. Bertrand, J. Carreaud, G. Delaizir, J.-R. Duclère, M. Colas, J. Cornette, M. Vandenhende, V. Couderc, P. Thomas, A comprehensive study of the carbon contamination in tellurite glasses and glass-ceramics sintered by SPS, J. Am. Ceram. Soc. 97 (1) (2014) 163–172.
[38] S.F. Mayer, H. Falcón, M.T. Fernández-Díaz, J.A. Alonso, The crystal structure of defect KBB'O_6 Pyrochlores (B,B': Nb,W,Sb,Te) revisited from Neutron Diffraction Data, Crystals 8 (10) (2018) 368.
[39] A.V. Knyazev, W. Paraguassu, A.G. Blokhina, M.I. Lelet, S.S. Knyazeva, G.B. Corrêa Junior, Thermodynamic and spectroscopic properties of $KNbTeO_6$, J. Chem. Thermodyn. 107 (2017) 26–36.
[40] T. Siritanon, J. Li, J.K. Stalick, R.T. Macaluso, A.W. Sleight, M.A. Subramanian, $CsTe_2O_{6-x}$: novel mixed-valence tellurium oxides with framework-deficient pyrochlore-related structure, Inorg. Chem. 50 (17) (2011) 8494–8501.
[41] O. Yeheskel, O. Tevet, Elastic moduli of transparent yttria, J. Am. Ceram. Soc. 82 (1) (1999) 136–144.
[42] M. Udovic, M. Valant, D. Suvorov, Phase formation and dielectric characterization of the Bi_2O_3–TeO_2 system prepared in an oxygen atmosphere, J. Am. Ceram. Soc. 87 (4) (2004) 591–597.